IMPACT STUDIES OF FIVE CERAMIC MATERIALS AND PYREX

J. E. REAUGH, A. C. HOLT, M. L. WILKINS, B. J. CUNNINGHAM, B. L. HORD, and A. S. KUSUBOV

Lawrence Livermore National Laboratory Livermore, CA 94551

Summary—We measured the ballistic performance of five ceramic materials (alumina, silicon carbide, boron carbide, aluminum nitride, and titanium diboride) and Pyrex, when they are backed by thick steel plates. The projectile for all tests was a right-circular cylinder of tungsten sinter-alloy W2 with length 25.4 mm and diameter 6.35 mm, fired at velocities from 1.35 to 2.65 km/s. For this threat we determined the minimum areal density of each material that is needed to keep the projectile from penetrating the backup steel. For all of the facing materials studied here, this performance measure increases approximately linearly with projectile velocity. However, the rate of increase is significantly lower for aluminum nitride than for the other materials studied. Indeed, aluminum nitride is a poor performer at the lowest velocity tested, but is clearly the best at the highest velocity. Our computer simulations show the significant influence of the backing material on ceramic performance, manifested by a transition region extending two projectile diameters upstream from the material interface. Experiments with multiple material layers show that this influence also manifests itself through a significant dependence of ballistic performance on the ordering of the material layers. © 1999 Elsevier Science Ltd. All rights reserved.

INTRODUCTION

Ceramics, when used appropriately, can stop a variety of projectiles with less weight per unit area than ballistic steel. The design of ceramic composite armor to stop projectiles and the design of laboratory targets to examine the ballistic behavior of ceramic materials is complicated by the characteristic properties of ceramics — strength in compression and weakness in tension. In the late 60's and early 70's, Wilkins and colleagues[1-5] demonstrated that both properties are important to the defeat of small caliber (7.6 mm) armor-piercing projectiles, and that no single property would correlate ballistic performance for all scenarios. His observations explained why different laboratory targets, which are intended to examine ceramic behavior and which may weight tensile and compressive behavior differently, can produce different rankings among the candidate facing materials. The implication is that one who wishes to measure the ballistic performance of ceramics needs to consciously select a target configuration and projectile combination that tests the particular properties of interest.

For the study reported here, we chose a target configuration that is simple, and that tests the behavior of a facing material when it is well-supported by thick ballistic steel. This eliminates the complex influence of back-plate flexure on ceramic performance.

The projectile chosen is not intended to mimic any specific fielded projectile. It has an aspect ratio (L/D, where L is the projectile length and D is the projectile diameter) of 4, which is intermediate between short projectiles and long rods. It exhibits features of both long rods (quasi-steady penetration) and short projectiles (unsteady end-of-penetration described by Wilkins and Reaugh[6]) With this choice, we were able to defeat the projectile in the velocity range of interest with tile thicknesses of less than about half the lateral dimensions of the tiles available to us.

Table 1. Densities and sound velocities of ceramic facing materials

Ceramic	Longitudinal velocity[a], km/s	Shear velocity[a], km/s	Density, g/cc
Alumina AD96	10.10	5.97	3.75
Alumina AD85	8.80[c]	5.07	3.40
SiC	11.76	7.51	3.16
B4C	13.83	8.72	2.51
AlN	10.76	6.33	3.25
TiB$_2$	11.08	7.43	4.49
Pyrex	5.64[b]	3.28[b]	2.23

[a] Averaged from several samples of varying thickness
[b] From the AIP handbook, Ref. [7]
[c] From Ref. [3]

EXPERIMENTAL PROCEDURE

Our targets consisted of square tiles of facing material, 102 mm on a side, bonded onto the face of square steel backup plates, 152 mm on a side and 64 mm thick. A photograph of a typical target is shown in Fig. 1. The ceramic tiles were supplied by Dow Chemical Corporation. The Pyrex was of commercial grade. Densities and sound velocities of the facing materials are given in Table 1. We chose 4340 steel hardened to Rc35 as our backing material. This steel was chosen over rolled homogeneous armor (RHA) to eliminate the variability in mechanical properties that we have experienced in RHA in the past. The measured harnesses of our steel backing plates varied from Rc33 to Rc37. The other mechanical properties of the backing steel are given in Appendix B. We expect that the performance of the ceramic facings on this steel will be the same as on RHA. In preparation for target assembly, one side of each steel backup plate was milled lightly to insure a flat, clean and slightly roughened mounting surface. Tile surfaces to be bonded were ground flat and parallel to a tolerance of less than 0.03 mm. Surfaces to be bonded were cleaned with hexane to remove any traces of grease. To insure optimal bonding strength the steel block and ceramic tiles to be assembled were heated to approximately 40° C using infrared lamps. The components of the adhesive, Stycast 1266, were carefully weighed, mixed, and applied to the prepared surfaces. The tiles were then placed on the center of the backup plates. In some cases a single tile was used to produce a target. In others, several tiles were stacked to yield the required facing thickness. Thirty pound weights were placed on top of the tiles being glued to insure a minimal, adhesive layer thickness between the surfaces. The assemblies were then allowed to cure for 24 hours before they were handled. The projectile was a right circular cylinder, D=6.35 mm, and L=25.4 mm of tungsten sinter-alloy W2, manufactured by GTE. The manufacturer's technical specifications for the mechanical properties of W2 are given in Table 2.

Table 2. Material properties of W2 Tungsten alloy

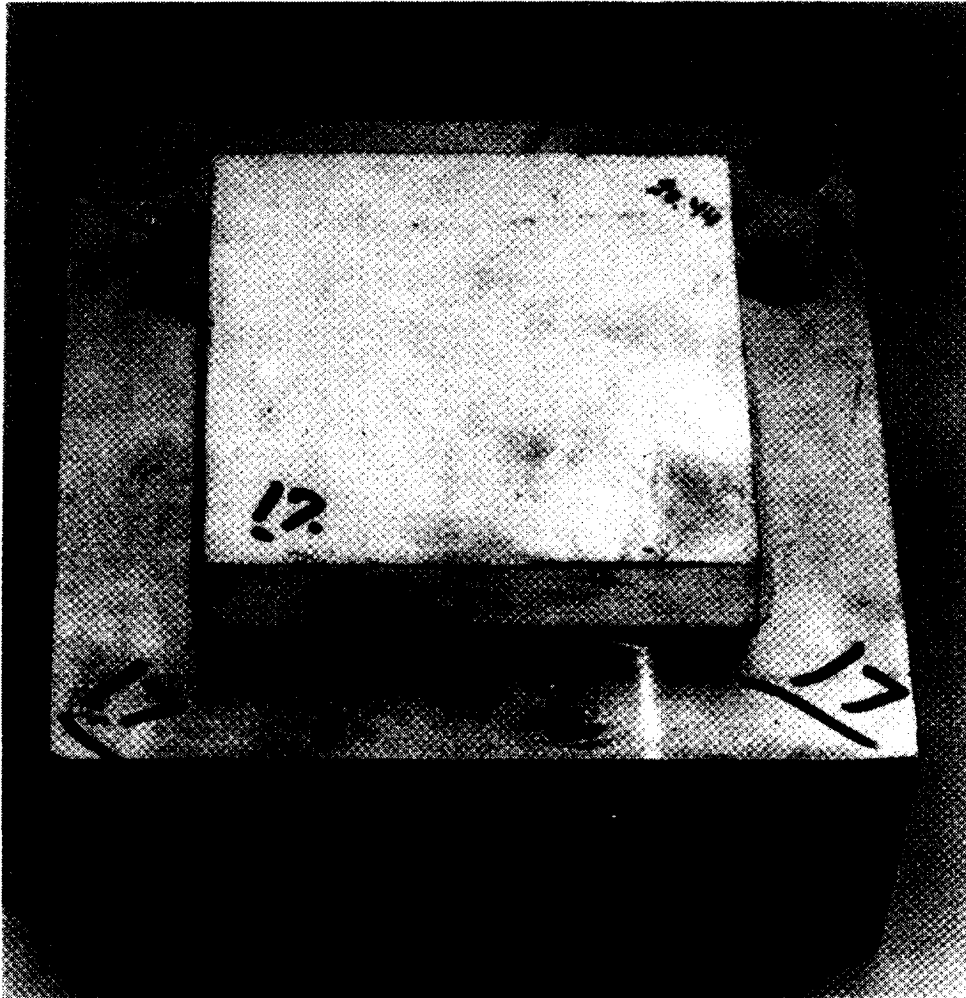| Property	Value
Density g/cc	18.36
Hardness, Rc	28 to 31
Ultimate tensile strength, kbar	8.80
Yield strength, kbar	6.95
Elongation at failure, %	5.5

Fig. 1. Target assembly with ceramic tile bonded to the face of a 4340 steel backup plate.

Our experiments were performed at three nominal velocities: 1.35, 1.75, and 2.6 km/s. The experiments at 1.35 and 1.75 km/s were performed using a 14.5 mm powder gun and a 23 mm powder gun respectively, at our ballistic range facility. The Lawrence Livermore National Laboratory two-stage light gas gun was used to accelerate the projectiles for the 2.6 km/s experiments. The shots at 1.35 km/s were fired into air at 1 atmosphere. In the other shots, the projectiles were fired into a vacuum of about 1 Tor. The sabot assembly was stripped from the projectile by a block of low-density foam. Flash x-rays were used to determine tilt and projectile velocity, as well as to verify that the sabot assembly had been separated from the projectile. Average projectile tilt for a representative sample of experiments was less than 2 degrees. Any tilt greater than 4 degrees was considered excessive and the experiment was repeated.

The depth of penetration into the steel backup plate, normal to the impact surface, P_b, was used as a performance measure for each shot. Two methods were used for measuring P_b. The first consisted of measuring the perpendicular distance form the upper surface of the block to the bottom of the crater using a micrometer depth gauge. An inverted U-shaped spacer was employed to straddle the distorted region around the crater opening and to facilitate referencing to the undistorted region of the front face. After measuring the distance from the top of the spacer

Table 3. Linear regression fit to normal impact data, $P_b = P_0 - a\Delta$, for values of the tile thickness Δ exceeding 10 mm. The average velocity of the experiments used for the fit is v.

	Low velocity			Intermediate velocity			High velocity		
Tile	P_0 mm	a	v, km/s	P_0 mm	a	v, km/s	P_0 mm	a	v, km/s
AD85	17.7	0.44	1.36	31.2	0.68	1.76	50.8	0.80	2.50
AD96	19.5	0.52	1.36	31.3	0.77	1.70	54.1	0.93	2.63
AlN	18.0	0.68	1.29	36.4	1.01	1.79	55.5	1.20	2.60
B_4C	33.9	1.98	1.25	38.9	1.01	1.77	32.1	0.45	2.61
Pyrex	---	---	---	33.2	0.59	1.79	53.2	0.63	2.65
SiC	37.2	2.33	1.37	35.5	1.05	1.72	38.9	0.64	2.65
TiB_2	44.2	4.05	1.35	41.6	2.09	1.70	60.4	1.30	2.65

to the bottom of the crater, the spacer thickness was subtracted to give the hole depth. The end of the depth gauge used is flat with a diameter of 3.2 mm. If the crater was too deep for the first method, or if it were suspected that significant amounts of residual penetrator was present at the bottom of the crater, the steel block was sectioned. Normal depth of penetration was then determined by using a caliper to measure the distance from the deepest point of the projectile penetration to the rear surface of the backup plate and subtracting that value from the (undistorted) backup plate thickness.

EXPERIMENTAL RESULTS

Our measured values of P_b are given in Appendix A. Since we measured the penetration depth into the backup plate as a function of facing thickness, we can estimate the minimum facing thickness necessary to prevent penetration of the backup plate, Δ^*. To this end, we performed a linear regression fit of P_b as a function of facing thickness for each material at each nominal velocity. The fit can then be used to solve for Δ^*. The results are given in Table 3, and plotted in Fig. 3. In that figure we see that the limiting areal density for each ceramic increases approximately linearly with velocity, and that the various ceramics have different rates of increase. In particular, the limiting areal density of aluminum nitride has the slowest increase with velocity of all the materials tested. As a consequence, it is the best of the ceramics tested at high velocity, i.e. requires the least areal density to stop the projectile.

We wondered whether stacking several facing plates to obtain a desired thickness would give a different result in our experiments than if the facing had been a single plate of the same thickness as the total. In order to investigate this question, we repeated the silicon carbide shot at 1.75 km/s with 20 mm of facing. In the original shot, we used a single 20 mm thick tile as facing, and in the second, we stacked two 10 mm plates. The difference in the results was insignificant.

Our simulations, discussed below, suggested that if two layers of different facing materials are used over the steel backup plate, then the order in which they occur might strongly influence their performance. In order to see if this is so, we performed a series of experiments in which titanium diboride plates were used in combination with Pyrex and with AD96 plates. In each case, shots were performed with the TiB_2 next to the steel and then again, with the TiB_2 on the front face. The results of these experiments are given in Table 4. They show a strong dependence on the ordering of the facing materials.

With thin (10mm) tiles of AD96 and TiB_2, the residual penetration is slightly smaller when the TiB_2 is on the outside (Table 4) although the difference is small, 14 versus 16 mm. At equal areal density, an all-AD96 tile would result in the same residual, 15.6 mm, but an all-TiB_2 tile would result in only 5 mm. The thin TiB_2 tile does not perform well. With thicker tiles of TiB_2 and Pyrex the order is more significant. (Table 4) At equal areal density, an all-Pyrex tile would result in 7 mm residual, whereas an all-TiB_2 tile would stop the projectile (no residual). The
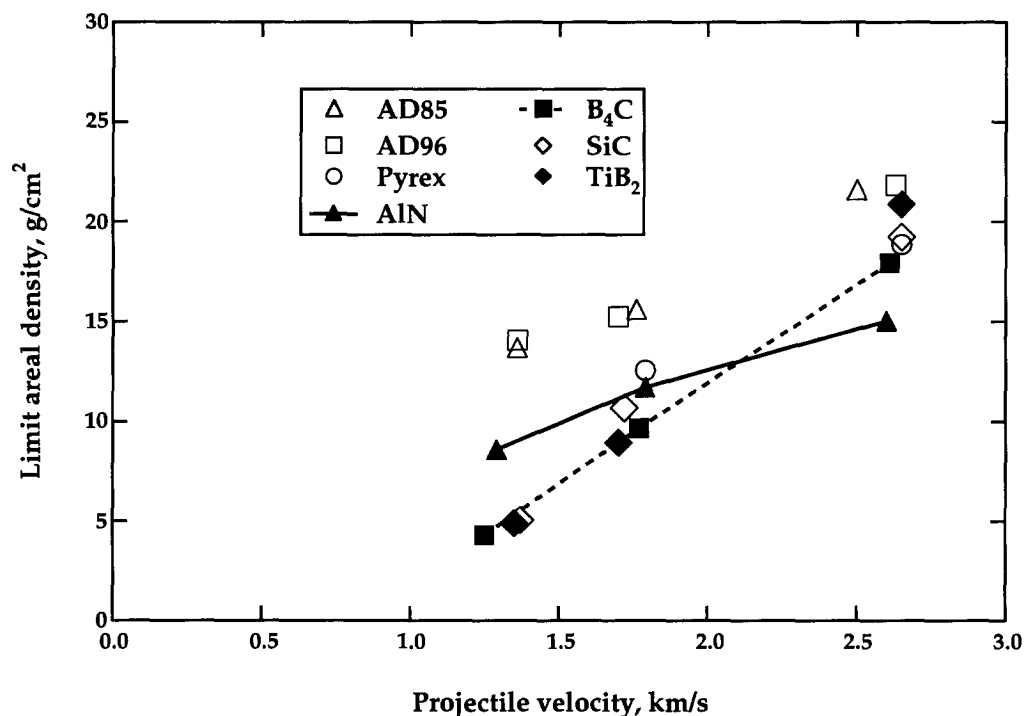
Fig. 3. The limit areal density required to prevent penetration in the backup steel, calculated from fits to the experimental data. The AlN limit value increases slowly with velocity.

combination with Pyrex on the outside has higher residual penetration than either single-material facing. With TiB_2 on the outside, the combination results in less residual than all Pyrex, but more than all-TiB_2. The thin TiB_2 tile performs as badly with thicker Pyrex backing as it does with AD96 backing.

Table 4. Experimental results for 25.4 mm by 6.35 mm diameter tungsten cylinder into steel faced by multiple ceramic plates at normal obliquity.

Upper plate		Lower plate		Projectile	Penetration
Material	Thickness, mm	Material	Thickness, mm	velocity, km/s	into steel, mm
AD96	10.2	TiB_2	10.0	1.78	16.1
TiB_2	10.1	AD96	10.2	1.76	13.9
Pyrex	13.7	TiB_2	14.8	1.78	12.6
TiB_2	14.7	Pyrex	13.8	1.77	4.8
TiB_2	10.0	Pyrex	18.5	1.77	11.9

COMPUTER SIMULATIONS

We performed computer simulations of some of the experiments using GLO, a two-dimensional multi-material Eulerian finite-difference code under development at our laboratory. The material parameters used to model the 4340 steel backing are those for Rc35 steel given in Appendix B.

Simulations with Pyrex

We selected Pyrex as the first tile material for the simulations. Previous experimental results suggested that the Pyrex fractures and breaks early in the penetration event, and so could be modeled as a broken material throughout the penetration event.

By assuming this, we achieve a significant simplification in the task of modeling ceramics numerically. The reason is that the change in the state from intact to broken is accompanied by a significant reduction in the magnitude of stress, whether fracture takes place in compression or tension. The resulting release of strain energy is propagated through the system with amplitude and period that are proportional to the finite-difference zone size. This numerical noise will, if the zone size is too large, be of sufficient amplitude to trigger the fracture of nearby zones. In contrast, when the material is in a single state (for Pyrex, always broken) the numerical solution is smooth.

The behavior of broken, hard materials is described by the Mohr-Coulomb friction model for granular media, well-known in the literature of soil and rock mechanics (for example[8]). The difference between the maximum principal stress, σ_1, and the minimum principal stress, σ_3, is given by

$$\sigma_1 - \sigma_3 = (\sigma_1 + \sigma_3)\sin\varphi \tag{1}$$

where positive stress is compressive, and φ is the friction angle. A somewhat simpler implementation, which does not require calculation of the principal stresses, is the extended von Mises criterion[8]

$$Y = \alpha P \tag{2}$$

where Y is the equivalent stress and P is the mean stress. When this criterion is fit to the compressive triaxial test ($\sigma_1 > \sigma_2 = \sigma_3$), where σ_2 is the intermediate principal stress, it overestimates the measured strength of granular materials in shear ($\sigma_2 = 0$) and extension ($\sigma_1 = \sigma_2 > \sigma_3$). Nevertheless, we used this latter criterion (Eq. 2) in our computer simulations. So long as the parameter α is less than 1.5, the minimum principal stress is never in tension.

A second feature that accompanies the shear of granular material is dilatency[9], the increase in volume observed when a mass of dense, granular material undergoes shear at constant confining pressure. Although the plastic potential theory of von Mises will generate a plastic volume increase during shear deformation when the extended von Mises criterion (Eq. 2) is used as the potential surface, we have chosen to ignore dilatency. Experiments on granular soils[10] show that there is a characteristic porosity, which is a function of confining stress, that is achieved by a soil mass undergoing large shear deformation. In contrast, naive use of the plastic potential theory (associated flow rule) produces ever-increasing volume with shear deformation at constant normal stress. More complicated flow rules (or more complicated limit surfaces) are required to obtain physically realistic results, and require the specification of additional parameters.

We found the parameter α in the extended von Mises criterion by the expedient of matching results of numerical simulations to experiments by Hord[11], in which a short W2 projectile (L/D = 2.5) was fired into a confined Pyrex column at 1.5 km/s. Flash x-rays were taken during the penetration event to mark the nose and tail position. Results of the experiments and two computer simulations with different values of α are shown in Fig. 4. The final positions and residual projectile lengths are shown also. We chose $\alpha = 0.8$ for the remainder of the computer simulations for Pyrex. Similar experiments in glass with a longer rod were performed by Hohler and Stilp. Calculations of those experiments and the experimental results are reported by Anderson *et al.*[12]

Table 5. Calculated influence of the backing metal on the performance of 20 mm thick Pyrex tiles at 1.75 km/s

Backing metal	P_{0B}, mm^a	P_B, mm	$\eta_M{}^b$	$\eta_{MS}{}^c$
Aluminum	82.5	58.0	1.5	1.9
Steel	36.0	21.2	2.6	2.6
Tungsten	20.6	11.1	3.9	2.9

[a] P_{0B} is the penetration in the backing metal without Pyrex
[b] The differential efficiency, η_M is given by

$$\eta_M = \rho_B (P_{0B} - P_B)/(\rho_C\Delta)$$

where ρ_B is the backing metal density, ρ_C the tile density, and Δ the tile thickness..
[c] The differential efficiency scaled to steel, η_{MS}, is given by

$$\eta_{MS} = \rho_S P_{0S}/(\rho_B P_{0B})$$

where ρ_S is the density of steel and P_{0S} the penetration in steel alone.

With this model for Pyrex, we performed computer simulations of the experimental geometry at 1.75 km/s, in advance of experiments with Pyrex. The comparison of the computed and measured residual penetration in steel is shown in Fig. 5. The good agreement with experiment led us to examine the results of the computer simulations in more detail.

We show the velocity at the projectile nose and tail as a function of the nose position in Fig. 6. There is a noticeable change in the nose (interface) velocity from the value characteristic of Pyrex to the value characteristic of steel over a distance in Pyrex that is approximately two projectile diameters. When we repeated the calculations, replacing the steel backup with aluminum and with tungsten, the transition region had the same two-diameter thickness, but with the final interface velocity being characteristic of aluminum or tungsten as can be seen in Fig. 7. This transition region has a significant effect on the differential efficiency of Pyrex, even when scaled to steel for all cases (Table 5.)
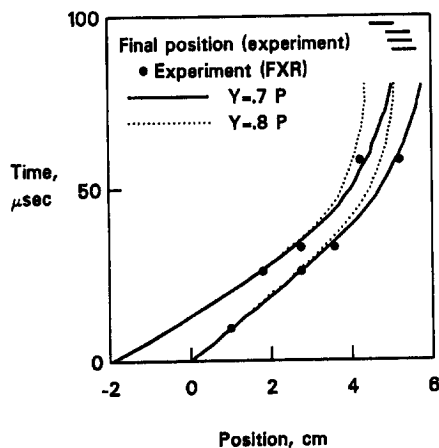

Fig. 4. Position of nose and tail as functions of time from experimental flash x-rays (solid dots) and simulations (solid and dashed lines). Final position and residual length shown by short lines at the top
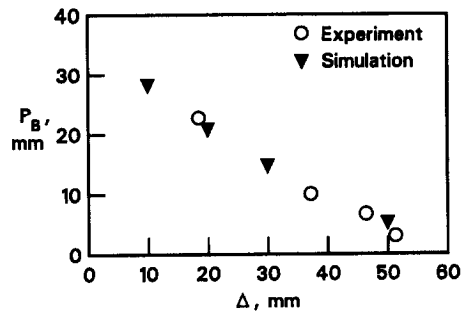
Fig. 5. Residual penetration in the back-up steel as a function of Pyrex thickness from experiment and simulation
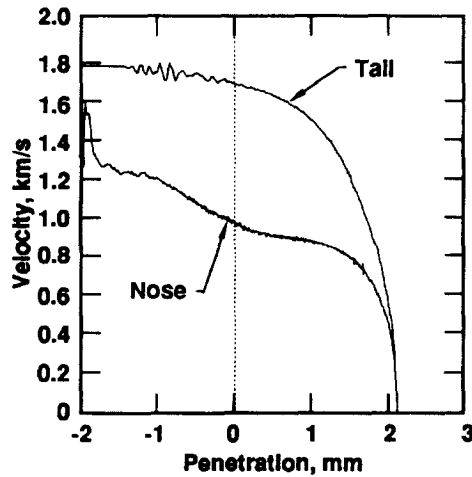
Fig. 6. Calculated nose and tail velocities as a function of nose position in a 20mm Pyrex/steel target. Original position of the interface is at zero.
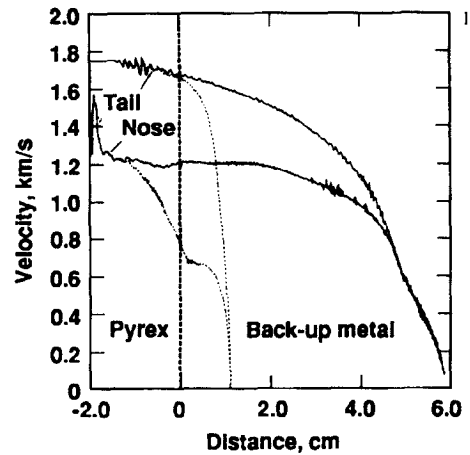
Fig. 7. Calculated nose and tail velocity as a function of nose position for a 20mm Pyrex/metal target using aluminum (solid) and tungsten (dash) to replace steel.

Simulations with Aluminum Nitride

The experimental results with aluminum nitride sufficiently intrigued us that we sought to model those experiments as well. Heard and Cline[13] showed a transition from brittle to ductile failure in quasi-static triaxial compression tests when the confining stress $\sigma_2 = \sigma_3$ exceeded 6 kbar (pressure about 20 kbar). This suggested to us that perhaps at the highest velocity experiments, the mean stress in aluminum nitride was sufficiently large that the material was ductile, even at the strain rates of the impact test $(10^5/s)$. We fit the quasi-static data[13] by an extended von Mises surface Y = f(P), and estimated the strength at the Hugoniot elastic limit to be 68 kbar, as shown in Fig. 8. Figure 9 shows the interpolated/extrapolated experimental penetration in the backup steel as a function of velocity for a 20 mm tile of AlN, together with calculations using the intact strength and the broken strength, where the value of α for broken AlN was arbitrarily taken to be the same value as was used for glass (Fig. 8).

From these results, it is our assessment that AlN is behaving substantially like a broken material at the lower two velocities, although we cannot rule out the possibility that there is a short time when the material retains its intact strength. In any event it is apparent that the calculations using the intact strength of AlN are incorrect at the lower two velocities.

When we examine detailed results of the two lower-velocity calculations that used the intact strength, the first 10% of plastic strain experienced by material in the path of the projectile is achieved at pressures below 30 kbar. At the strain rates achieved in the ballistic test, $10^5/s$, we would estimate the brittle-ductile transition to occur at 30 to 40 kbar (20 kbar for the quasi-static tests). Thus we would infer that at the lower two velocities, the AlN fractures and is broken in the penetration path. The case for the higher velocity is less clear-cut. Most of the strain is achieved at pressures exceeding 35 kbar, although the strain from 2 to 4% is achieved at pressures as low as 25 kbar. At somewhat higher velocity, 3.5 km/s, we would anticipate that AlN in the penetration path would behave as a ductile, high strength material, and exhibit excellent resistance to penetration.

The calculations using the extended von Mises criterion for broken AlN are also not accurate except at the intermediate velocity. We note that the value of α chosen was the one for Pyrex, which gives results in substantial agreement with experiment in the velocity range 1.5 to 1.75 km/s, but is otherwise unsupported by independent experiment at different velocities (or confining pressure).
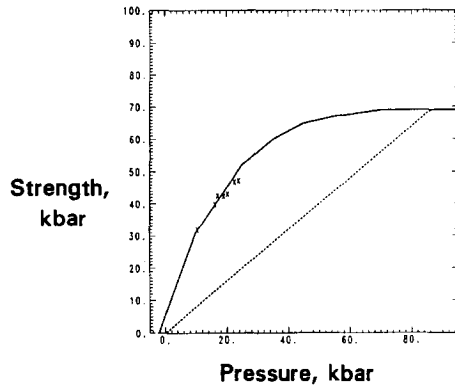
Fig. 8. Measured strength of aluminum nitride (x) and model fit for intact (solid) and broken AlN. The slope for the broken material is the same as was used for Pyrex.
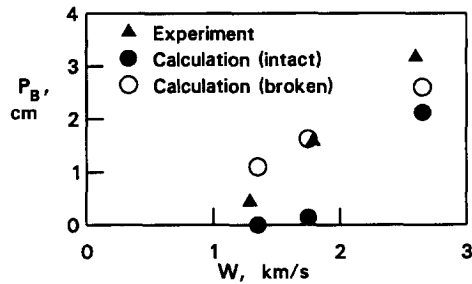
Fig. 9. Penetration in the back-up steel as a function of velocity for 20mm AlN/steel target from experiment and simulations

CONCLUDING REMARKS

Our experimental results show that titanium diboride, boron carbide, and silicon carbide. perform equally well when supported by a thick steel backing. They outperform aluminum nitride, Pyrex, and alumina at velocities below 2.0 km/s. Interestingly, the two aluminas have about equal performance in this ballistic test for all three velocities.

At velocities above about 2.0 km/s the aluminum nitride outperforms all the others. Moreover, Pyrex ranks with boron carbide, titanium diboride and silicon carbide at about 2.6 km/s and may outperform them at higher velocities. Our computer simulations for aluminum nitride suggest to us that the superior performance of aluminum nitride at the highest velocity is due to its retention through ductility of a substantial part of its strength at the high confining pressures experienced there, in contrast to the other ceramics, which are substantially broken at high velocity.

Our simulations of the Pyrex experiments show that a target material interface begins to influence the penetration process when the projectile nose is yet a significant distance away. This observation explains why thin layers of a facing material do not perform the same way as thicker ones. It is because the process is entirely within the transition region, where both materials are influencing the penetration process.

APPENDIX A. RESIDUAL NORMAL PENETRATION IN STEEL

We present the experimental results for the normal residual penetration of a 6.35-mm diameter by 25.4-mm long tungsten projectile into the back-up steel. In the table below, the tile thickness, Δ, is in mm, the projectile velocity, V, is in km/s, the obliquity, θ, in degrees between the flight axis and the normal to the tile. The residual penetration in the backup steel normal to the steel surface, P_b, is in mm.

Table A1. Experimental residual penetration

Tile	Δ	V	θ	P_b	Tile	Δ	V	θ	P_b
AD96	10.5	1.35	0	14.5	AD85	6.2	1.33	0	18.5
AD96	15.1	1.35[a]	0	11.1	AD85	14.0	1.35	0	11.8
AD96	20.6	1.36	0	8.7	AD85	22.1	1.35	0	7.5
AD96	30.2	1.36	0	4.0	AD85	32.0	1.37	0	3.8
AD96	20.4	1.68	0	15.8	AD85	6.2	1.75	0	31.0
AD96	31.7	1.72	0	6.4	AD85	14.0	1.75	0	22.0
AD96	40.0	1.70	0	0.0	AD85	29.9	1.75	0	10.0
AD96	40.4	1.80	0	0.5	AD85	42.5	1.77	0	2.7
AD96	15.1	1.69	30	14.0	AD85	20.5	2.50	0	33.6
AD96	29.9	1.74	30	5.5	AD85	39.3	2.50	0	20.6
AD96	15.3	1.80	45	9.5	AD85	59.1	2.50	0	2.6
AD96	25.0	1.72	45	0.0	SiC	10.0	1.37	0	13.9
AD96	10.5	1.74[a]	60	6.7	SiC	15.1	1.36	0	2.0
AD96	15.2	1.74[a]	60	4.1	SiC	20.0	1.37	0	0.0
AD96	20.0	1.74	60	0.0	SiC	30.1	1.31	0	0.0
AD96	15.1	2.63	0	39.2	SiC	20.0[b]	1.69	0	14.3
AD96	30.1	2.63	0	27.8	SiC	20.0[b]	1.75[a]	0	14.5
AD96	51.3	2.62	0	5.9	SiC	29.5	1.77	0	5.7
TiB$_2$	7.9	1.38	0	12.2	SiC	30.2	1.70	0	2.4
TiB$_2$	10.0	1.31	0	3.7	SiC	40.0	1.74	0	0.0
TiB$_2$	15.0	1.36	0	0.0	SiC	15.0	1.75	30	14.9
TiB$_2$	20.0	1.37	0	0.0	SiC	31.3	1.78	30	1.0
TiB$_2$	10.1	1.69	0	22.1	SiC	15.1	1.71	45	8.2
TiB$_2$	14.9	1.70	0	7.3	SiC	25.0	1.81	45	0.0
TiB$_2$	20.1	1.72	0	1.1	SiC	10.1	1.70	60	6.6
TiB$_2$	30.0	1.69	0	0.0	SiC	14.9	1.80	60	1.9
TiB$_2$	10.1	1.70	30	19.5	SiC	20.0	1.69	60	0.0
TiB$_2$	25.0	1.80	30	0.0	SiC	30.1	2.62	0	18.2
TiB$_2$	7.7	1.73	45	15.4	SiC	39.9	2.68	0	15.6
TiB$_2$	20.0	1.69	45	0.0	SiC	59.7	2.64	0	0.
TiB$_2$	7.8	1.80	60	5.6	B$_4$C	10.4	1.79	0	28.3
TiB$_2$	15.0	1.81	60	0.0	B$_4$C	19.3	1.74[a]	0	19.8
TiB$_2$	20.1	2.63	0	34.5	B$_4$C	28.8	1.78	0	9.8
TiB$_2$	24.9	2.69	0	29.8	B$_4$C	28.0	1.79	30	3.3
TiB$_2$	30.3	2.63	0	17.8	B$_4$C	17.6	1.77	60	2.2
TiB$_2$	40.0	2.63	0	9.6	B$_4$C	10.4	1.28	0	13.3
AlN	9.7	1.25	0	10.1	B$_4$C	15.2	1.22	0	3.8
AlN	14.3	1.30	0	8.9	B$_4$C	19.2	1.29	0	0.0
AlN	19.6	1.31	0	4.3	B$_4$C	38.9	2.61	0	14.5
AlN	9.9	1.79	0	27.5	B$_4$C	58.6	2.61	0	5.6
AlN	19.7	1.79	0	14.3	Pyrex	18.5	1.80	0	22.7
AlN	28.8	1.80	0	8.5	Pyrex	37.2	1.78	0	10.0
AlN	37.0	1.79	0	0.0	Pyrex	46.4	1.78	0	6.7
AlN	28.2	1.76	30	1.6	Pyrex	51.3	1.80	0	3.0
AlN	17.5	1.78	60	0.0	Pyrex	39.4	2.64	0	28.5

Table A1. (concluded) Experimental residual penetration

Tile	Δ	V	θ	P_b	Tile	Δ	V	θ	P_b
AlN	30.3	2.61	0	19.3	Pyrex	58.9	2.65	0	16.3
AlN	39.5	2.58	0	8.3					

[a] Velocity estimated from the powder load

[b] The facing on the first of these two shots was a single 20 mm plate. The facing for the second was two 10 mm plates bonded together.

Table A2. Penetration depth of normal impacts into the back-up steel alone.

V	P_b
1.34[a]	26.8
1.34	27.0
1.34	27.0
1.35	27.8
1.35	28.5
1.74[a]	35.3
1.77	36.0
2.50	43.8

[a] Velocity estimated from the powder load

APPENDIX B. CHARACTERIZATION OF 4340 STEEL

Four-inch diameter billets of 4340 steel were quenched and tempered to achieve nominal Rockwell hardness of Rc35, Rc40, and Rc45. Three 0.5-inch diameter standard tensile specimens (2-inch gauge length, 6 inches long) were machined from each heat treatment, designated 35-1, 35-2, 35-3, 40-1, etc. The specimens were tested in tension on a 56,000 pound Instron machine according to ASTM standard E8 at room temperature. Crosshead speed was 0.01 in/min., except for specimens 35-1, 35-2, 40-1, and 45-1, which were tested at 0.005 in/min. Gauge extension was measured with an Instron 2"-50% extensometer, and load-elongation plots were produced for each test. In addition, a Zygo laser was used to scan 1.7 inches of the 2-inch gauge length at a speed of 0.26 in/s on an interval determined by the deviation of the minimum diameter from the original diameter, ranging from once every five minutes initially to once every 20 sec when the diameter had reduced by 30%. During each sweep, approximately 90 diameter determinations were made and recorded digitally, together with the load at the beginning and end of each sweep.

Table B1. Parameters for the flow stress of 4340 Steel

Nominal hardness, Rc	Measured hardness, Rc	Y_0, kbar	β	n
35	34	10.3	125	0.0700
40	40	12.9	282	0.0389
45	43	13.2	580	0.0350

We followed the procedure of Norris et al.[15] to determine the work-hardening functional dependence of the three heat treatments. In that procedure, a computer simulation of the tension test is performed (we used HEMP[16]) with an initial guess at the work-hardening. Results of the computer simulations and experiments are compared, and the work hardening function revised until satisfactory agreement is reached. The results are shown in Fig. B1-B3 for the three heat treatments. In those figures true strain is -2 ln(D/D_0) where D is the minimum diameter.

Engineering stress is the load per unit area of the original minimum cross-section. The functional form chosen for the flow stress is

$$Y = Y_0(1 + \beta \varepsilon^p)^n \tag{B1}$$

where Y is the equivalent stress, and ε^p is the equivalent plastic strain. The fitted parameters are given in Table B1.
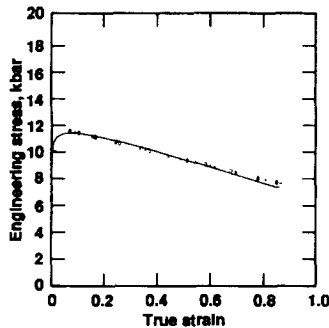

Fig. B1. Engineering stress as a function of true strain for 4340 steel, Rc35 for experiments (symbols) and simulation (line).
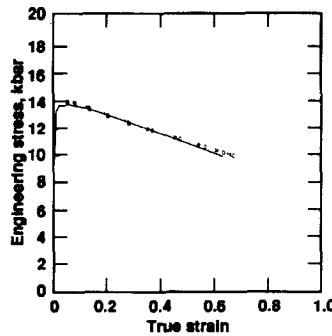
Fig. B2. Engineering stress as a function of true strain for 4340 steel, Rc40 for experiments (symbols) and simulation (line).
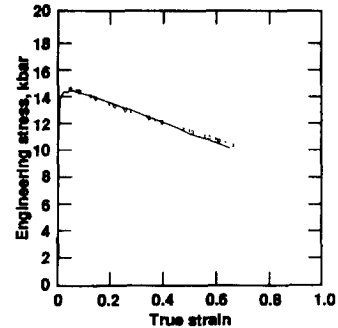
Fig. B3. Engineering stress as a function of true strain for 4340 steel, Rc45 for experiments (symbols) and simulation (line).

REFERENCES

1. M. L. Wilkins, C. Honodel, and D. Sawle, "An approach to the study of light armor," Lawrence Livermore National Laboratory, Livermore, CA Report No. UCRL-50284, June 13, 1967.

2. M. L. Wilkins, "Second progress report of the light armor program," Lawrence Livermore National Laboratory, Livermore, CA Report No. UCRL-50349 Rev. 1, 1967.

3. M. L. Wilkins, "Third progress report of the light armor program," Lawrence Livermore National Laboratory, Livermore, CA Report No. UCRL-50460, July 9, 1968.

4. M. L. Wilkins, C. F. Cline, and C. A. Honodel, "Fourth progress report of light armor program," Lawrence Livermore National Laboratory, Livermore, CA Report No. UCRL-50694, 1969.

5. M. L. Wilkins, "Mechanics of penetration and perforation," *Int. J. Engrg. Sci.*, vol. 16, pp. 793-807, 1978.

6. M. L. Wilkins and J. E. Reaugh, "Computer simulations of ballistic experiments," Lawrence Livermore National Laboratory, Livermore, CA Report No. UCRL-95774, January 23, 1987.

7. D. E. Gray, "American Institute of Physics Handbook," , Third ed. New York: McGraw Hill Book Company, 1972.

8. A. W. Bishop, "Shear strength parameters for undisturbed and remoulded soil specimens," in *Stress-Strain Behavior of Soils*, R. H. G. Parry, Ed. Henly-on-Thames: G. T. Foulis & Co. Ltd., 1972, pp. 7-11.

9. O. Reynolds, "On the dilatency of media composed of rigid particles in contact, with experimental illustrations," *Phil. Mag. S.*, vol. 5, pp. 20, 1885.

10. C. P. Wroth and R. H. Bassett, "A stress-strain relationship for the shearing behavior of a sand," *Geotechnique*, vol. 15, pp. 32-56, 1965.

11. B. L. Hord, Personal Communication, 1986.

12. C. E. Anderson, V. Hohler, J. D. Hohler, and A. J. Stilp, "Time-resolved Penetration of Long Rods into Glass Targets," *Int. J. Impact Engng.*, vol. submitted, 1998.

13. H. C. Heard and C. F. Cline, "Mechanical behavior of polycrystalline BeO, Al_2O_3 and AlN at high pressure," *Mats. Science*, vol. 15, pp. 1889-1897, 1980.

14. D. J. Steinberg and R. E. Tipton, "A new fracture model for ceramics," Lawrence Livermore National Laboratory, Livermore, CA Report No. UCRL-JC-116953, March 14, 1994.

15. D. N. Norris, B. Moran, J. K. Scudder, and D. F. Quinones, "A computer simulation of the tension test," *J. Mech. Phys. Solids*, vol. 26, pp. 1-19, 1968.

16. M. L. Wilkins, "Calculation of Elastic-Plastic Flow," in *Methods of Computational Physics*, vol. 3, B. Alder, S. Fernbach, and M. Rotenberg, Eds. New York: Academic, 1964, pp. 211-263.